

# Merger and Mass Ejection of Neutron Star Binaries

Masaru Shibata<sup>1,2</sup> and Kenta Hotokezaka<sup>3</sup>

<sup>1</sup>Max Planck Institute for Gravitational Physics (Albert Einstein Institute), D-14476 Potsdam-Golm, Germany

<sup>2</sup>Center for Gravitational Physics, Yukawa Institute for Theoretical Physics, Kyoto University, Kyoto 606-8502, Japan; email: mshibata@yukawa.kyoto-u.ac.jp

<sup>3</sup>Department of Astrophysical Sciences, Princeton University, Princeton, New Jersey 08544, USA

**ANNUAL  
REVIEWS CONNECT**

[www.annualreviews.org](http://www.annualreviews.org)

- Download figures
- Navigate cited references
- Keyword search
- Explore related articles
- Share via email or social media

Annu. Rev. Nucl. Part. Sci. 2019. 69:41–64

First published as a Review in Advance on May 28, 2019

The *Annual Review of Nuclear and Particle Science* is online at [nucl.annualreviews.org](http://nucl.annualreviews.org)

<https://doi.org/10.1146/annurev-nucl-101918-023625>

Copyright © 2019 by Annual Reviews.  
All rights reserved

## Keywords

neutron star merger, black hole, neutron star, gravitational waves, electromagnetic counterparts, r-process nucleosynthesis

## Abstract

Mergers of binary neutron stars and black hole–neutron star binaries are among the most promising sources for ground-based gravitational-wave (GW) detectors and are also high-energy astrophysical phenomena, as illustrated by the observations of GWs and electromagnetic (EM) waves in the event of GW170817. Mergers of these neutron star binaries are also the most promising sites for r-process nucleosynthesis. Numerical simulation in full general relativity (numerical relativity) is a unique approach to the theoretical prediction of the merger process, GWs emitted, mass ejection process, and resulting EM emission. We summarize the current understanding of the processes of neutron star mergers and subsequent mass ejection based on the results of the latest numerical-relativity simulations. We emphasize that the predictions of the numerical-relativity simulations agree broadly with the optical and IR observations of GW170817.

## Contents

1. INTRODUCTION .....	42
2. SCENARIOS FOR NEUTRON STAR MERGER AND POSTMERGER .....	43
2.1. Binary Neutron Stars .....	44
2.2. Black Hole–Neutron Star Binaries .....	46
3. MASS EJECTION FROM NEUTRON STAR MERGERS .....	48
3.1. Dynamical Mass Ejection from Binary Neutron Stars .....	48
3.2. Dynamical Mass Ejection from Black Hole–Neutron Star Binaries .....	51
3.3. Viscosity-Driven Mass Ejection from Merger Remnants .....	51
3.4. Summary of Ejecta .....	52
4. ELECTROMAGNETIC COUNTERPARTS OF NEUTRON STAR MERGERS .....	52
4.1. r-Process Nucleosynthesis and Ejecta Opacity .....	53
4.2. Kilonovae (Macronovae) .....	53
4.3. Synchrotron Emission .....	56
5. GW170817 .....	58
5.1. Kilonova Observation .....	58
5.2. Synchrotron Emission and Jet .....	60

## 1. INTRODUCTION

Mergers of neutron star (NS) binaries [binary NSs and black hole–neutron star (BH-NS) binaries] are among the most promising sources of gravitational waves (GWs) for ground-based detectors, such as Advanced LIGO, Advanced Virgo, and KAGRA (1–3). Advanced LIGO and Advanced Virgo made the first observation of GWs from binary NSs on August 17, 2017 (GW170817) (4). We expect that these GW telescopes will detect a number of signals from NS binaries in the next few years.

NS mergers are also attracting attention as promising nucleosynthesis sites of heavy elements through the rapid neutron-capture process (r-process) (5–7), because a significant amount of neutron-rich matter is likely to be ejected during merger (see References 8–11 for the pioneering research). In association with the production of neutron-rich heavy elements in the merger ejecta, a strong electromagnetic (EM) emission (kilonova/macronova) is predicted to be powered by the subsequent radioactive decay of the r-process elements (12–18). This will be an EM counterpart of GWs from NS mergers, and its detection could be used to verify the NS merger scenario for the origin of r-process elements. This hypothesis has been strengthened by the observation of UV, optical, and IR signals of GW170817 (19–29). In addition to kilonovae, a long-lasting synchrotron emission at multiple wavelengths could arise from the interaction between the merger ejecta and the interstellar medium (ISM) (30). The detection of such signals is a unique probe to study the velocity profile of the merger ejecta. All these facts have encouraged the GW astronomy community to theoretically explore the mass ejection mechanisms, r-process nucleosynthesis, and associated EM emission in NS mergers.

To study these topics quantitatively, we must clarify the merger process, subsequent mass ejection, nucleosynthesis and subsequent decay of heavy elements in the ejecta, and EM emission arising from the ejecta. Numerical-relativity simulations that take into account the detailed microphysical processes, neutrino radiation transfer, and magnetohydrodynamics (MHD) are

currently our best approach to the problem. Considerable effort has been devoted to developing numerical-relativity simulations for NS mergers over the past two decades, since the first successful simulation of a binary NS merger in 1999 (31, 32). Now, detailed modeling for merger phenomena is feasible. In particular, during the last decade, researchers have performed a wide variety of numerical-relativity simulations, taking into account finite-temperature effects for NS equations of state (EOSs) (33, 34), neutrino cooling (34–37) and neutrino heating (38, 39), and MHD instability (40–42). Numerical relativity has become a robust tool to study merger phenomena, and it allows us to predict observational features of NS mergers.

The mass ejection processes have been explored with numerical-relativity simulations since the publications by Hotokezaka et al. (43) for binary NSs and by Foucart et al. (44) for BH-NS binaries [see also Bauswein et al. (45) for an approximately general-relativistic work]. A variety of numerical-relativity simulations have been performed to explore the nature of dynamical ejecta (37–39, 46–58). These publications have clarified that the mass of the dynamically ejected matter during merger depends strongly on the EOS, total mass and mass ratio of the system, and BH spin (for BH-NS binaries). For binary NSs, the ejecta components have a somewhat broad range of electron fraction between  $\sim 0.05$  and  $\sim 0.5$ , irrespective of the EOS (here the electron fraction, denoted by  $Y_e$ , is the electron number density per baryon number density). This broad  $Y_e$  distribution is well suited for explaining the abundance patterns of r-process elements with mass numbers larger than  $A \sim 90$  observed in the Solar System and metal-poor stars (52, 59). By contrast, for BH-NS binaries, the electron fraction of the dynamical ejecta is always low ( $Y_e \lesssim 0.1$ ); therefore, heavy r-process elements ( $A \gtrsim 130$ ) are dominantly synthesized (60).

After a binary NS merger, a BH or a massive neutron star (MNS) surrounded by a dense massive disk (or torus) is formed. Since 2013, various simulations of the evolution of such post-merger remnants have been performed (60–68). These simulations have indicated that a large fraction of mass of compact disks surrounding the central compact objects is ejected from the system by a viscous, nuclear recombination and/or the MHD effect. The mass of this ejecta can be of order  $10^{-2}M_\odot$ ; thus, it can dominate over the mass of dynamical ejecta, implying that this ejecta is as important as or even more important than dynamical ejecta to power EM emission.

The purpose of this article is to review the merger process and mass ejection mechanisms in NS merger and to summarize possible EM emission from the merger ejecta. This review is organized as follows. In Section 2, we summarize processes of the merger and postmerger phases of NS binaries based on the latest results of numerical-relativity simulations. In Section 3, we describe mass ejection processes during merger and from the postmerger remnants. In Section 4, we list the representative EM signals (UV, optical, IR, and radio signals) emitted from the ejecta of NS mergers. Finally, in Section 5, we note that the optical and IR signals of GW170817 are broadly consistent with the prediction by numerical relativity.

## 2. SCENARIOS FOR NEUTRON STAR MERGER AND POSTMERGER

The fate of NS mergers depends on the mass ( $m_1, m_2$ ) and spin of the binary components and on the NS EOS. For binary NSs, for which the effect of their spin is minor, the total mass ( $m = m_1 + m_2$ ), the mass ratio [ $q = m_2/m_1 (\leq 1)$ ] of the system, and the EOSs are the key quantities for determining the merger remnant. For BH-NS binaries, the BH spin as well as the mass ratio and NS EOS are the key quantities. In the following two subsections, we classify the remnants formed after NS mergers.

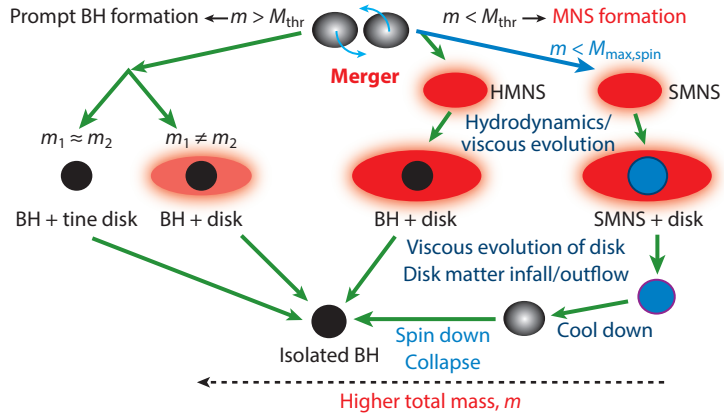


**Figure 1**

A summary of the merger and postmerger evolution of binary neutron stars.  $M_{\text{thr}}$  and  $M_{\text{max,spin}}$  denote the threshold mass for the prompt formation of a BH and the maximum mass of rigidly rotating cold neutron stars, respectively. Their values are likely to be  $M_{\text{thr}} \gtrsim 2.8M_{\odot}$  and  $M_{\text{max,spin}} \gtrsim 2.4M_{\odot}$ . For the total mass  $m > M_{\text{thr}}$ , a BH is formed in the dynamical timescale after the onset of merger, and for the nearly equal-mass case,  $m_1 \approx m_2$ , the mass of disks surrounding the BH is tiny,  $\ll 10^{-2}M_{\odot}$ , while it could be  $\gtrsim 10^{-2}M_{\odot}$  for a highly asymmetric system with  $m_2/m_1 \lesssim 0.8$ . For  $M_{\text{max,spin}} < m < M_{\text{thr}}$ , an HMNS is formed, and it subsequently evolves through several angular momentum transport processes, leading to its eventual collapse to a BH surrounded by a disk (or torus) (see References 69 and 70 for definitions of HMNS and SMNS). When  $m$  is close to  $M_{\text{thr}}$ , the lifetime of the MNS is relatively short, while for smaller values of  $m$  toward  $M_{\text{max,spin}}$ , the lifetime is longer. For the longer lifetime, the angular momentum transport process works for a longer timescale, and the disk mass could be  $\gtrsim 0.1M_{\odot}$ , whereas for a short lifetime, the mass could be  $\sim 10^{-2}M_{\odot}$  or less. For  $m < M_{\text{max,spin}}$ , an SMNS is formed, and it will be alive for a dissipation timescale of angular momentum that will be much longer than the cooling timescale,  $\sim 10$  s. Abbreviations: BH, black hole; HMNS, hypermassive neutron star; MNS, massive neutron star (either an HMNS or an SMNS); SMNS, supramassive neutron star.

## 2.1. Binary Neutron Stars

**Figure 1** summarizes the possible remnants and their evolution processes for mergers of binary NSs. Broadly speaking, there are two possible remnants formed immediately after the onset of merger: BH and MNS. A BH is formed if the total mass  $m$  is so high that the self gravity of the merger remnant cannot be sustained by the pressure associated primarily with the repulsive force among nucleons and centrifugal force due to rapid rotation associated with the orbital angular momentum of the premerger binary.

In the last decade, simulations were performed employing a variety of NS EOSs (e.g., 37–39, 43, 49, 52, 71–79), in which the maximum mass of a nonrotating NS is consistent with the existence of  $2M_{\odot}$  neutron stars (80, 81). An important finding of these simulations is that for  $m \lesssim 2.8M_{\odot}$  the remnant is, at least temporarily, an MNS and not a BH, regardless of the EOS employed.

The total mass of nine Galactic binary NSs for which the merger time is less than a Hubble time of  $\sim 13.8$  Gyr is in the range between  $\sim 2.50M_{\odot}$  and  $2.88M_{\odot}$  (82, 83). Among them, seven objects have a total mass smaller than  $2.75M_{\odot}$ , suggesting that, for the typical total mass of binary NSs, an MNS should be formed after merger (at least temporarily). In fact, the total mass of the binary NS GW170817 is in the middle of the above range,  $2.74^{+0.04}_{-0.01}M_{\odot}$ , for a low spin prior (4).

For  $m \gtrsim 2.8M_{\odot}$ , a BH could be formed immediately after merger, although the threshold mass for the prompt BH formation depends strongly on the EOS. The dimensionless BH spin,  $\chi$ , in the prompt BH formation case is  $\sim 0.8$  (73). The remnant BH in this formation channel is not

surrounded by a massive disk if the mass ratio,  $q$ , is close to unity. The mass of the disk surrounding the BH increases with the decrease of  $q$ , and in the presence of a significant mass asymmetry,  $q \lesssim 0.8$ , the disk mass could be  $\gtrsim 10^{-2} M_\odot$  (72, 73, 75). The disk is evolved by MHD processes, in particular by the effect of MHD turbulence induced by magnetorotational instability (MRI) (84) or the viscous process (see Section 2.2). During the MHD or viscous evolution of the disk, a short  $\gamma$ -ray burst (sGRB) may be launched from the vicinity of the BH by pair-annihilation processes of neutrinos emitted from the inner region of the disk (85–91) and/or by the effect of strong magnetic fields such as the Blandford–Znajek mechanism (92–95). The viscous angular momentum transport process also drives mass ejection in the viscous timescale of the disk (see Section 3 for details).

In the case of MNS formation, the MNS’s evolution is determined by several processes. Soon after the formation of the MNS, the gravitational torque associated with nonaxisymmetric structure of the merger remnant plays an important role in transporting angular momentum from the MNS to the surrounding matter (e.g., 75). This process reduces the angular momentum of the MNS. If it is marginally stable against gravitational collapse, the MNS collapses to a BH due to this process in  $\sim 10$  ms. The resulting system is a spinning BH of  $\chi \sim 0.6$ – $0.7$  surrounded by a disk of mass  $10^{-2}$ – $10^{-1} M_\odot$  (e.g., 50, 55).

On a longer timescale, viscous effects resulting from MHD turbulence are likely to play a key role in the evolution of the MNS (67, 96, 97). At its formation, the MNS is differentially rotating. Furthermore, it should be strongly magnetized and in an MHD turbulence state exciting a turbulent viscosity, because a velocity-shear layer is formed at the contact surfaces of the two merging NSs and the Kelvin–Helmholtz instability occurs (40, 41, 98, 99). This instability generates a number of small vortexes near the shear layer, and consequently, magnetic fields are wound up by the vortex motion, which enhances the magnetic-field strength on a timescale much shorter than the dynamical timescale of the system,  $\sim 0.1$  ms. Note that the growth timescale of the Kelvin–Helmholtz instability (100) is  $\tau_{\text{KH}} \sim 10^{-7} (\lambda/1 \text{ cm})$  ms for the wavelength  $\lambda$  because the typical velocity at the onset of merger is  $\sim 10^{10} \text{ cm s}^{-1}$ . Because of the presence of the differential rotation and turbulent viscosity, the angular momentum in the MNS should be transported outward, and as a result, the MNS is likely to settle into a rigidly rotating state (67, 96, 97). Simultaneously, a massive disk surrounding the MNS is formed because of the angular momentum transport. If this angular momentum transport significantly weakens centrifugal force in its central region, the MNS could collapse to a BH. Using the  $\alpha$ -viscous prescription for the turbulent viscosity (101), one can estimate the viscous timescale as

$$\tau_{\text{vis,MNS}} \approx 20 \text{ ms} \left( \frac{\alpha_{\text{vis}}}{10^{-2}} \right)^{-1} \left( \frac{c_s}{c/3} \right)^{-1} \left( \frac{R}{15 \text{ km}} \right)^2 \left( \frac{H}{10 \text{ km}} \right)^{-1}, \quad 1.$$

where  $\alpha_{\text{vis}}$  is the dimensionless viscous parameter,  $c_s$  is the sound velocity,  $c$  is the speed of light,  $R$  is the equatorial radius of the MNS, and  $H$  is the maximum size of the turbulent vortex. If a turbulent state is sufficiently developed, then  $\alpha_{\text{vis}}$  will become of the order  $10^{-2}$ , according to the latest results of high-resolution MHD simulations for accretion disks (102–104).

If the lifetime of the MNS is longer than  $\tau_{\text{vis,MNS}}$  (i.e., the MNS mass is not very large), then it will evolve through the viscous accretion from the disk and cooling by neutrino emission (67). The viscous timescale of the disk is written approximately as

$$\tau_{\text{vis,disk}} \approx 0.5 \text{ s} \left( \frac{\alpha_{\text{vis}}}{10^{-2}} \right)^{-1} \left( \frac{c_s}{c/10} \right)^{-1} \left( \frac{R_{\text{disk}}}{50 \text{ km}} \right) \left( \frac{H/R_{\text{disk}}}{1/3} \right)^{-1}, \quad 2.$$

where  $R_{\text{disk}}$  is the typical disk radius. The neutrino cooling timescale for MNSs is

$$\tau_\nu \approx \frac{U}{L_\nu} = 10 \text{ s} \left( \frac{U}{10^{53} \text{ erg}} \right) \left( \frac{L_\nu}{10^{52} \text{ erg s}^{-1}} \right)^{-1}, \quad 3.$$

where  $U$  is the thermal energy of the MNS and  $L_\nu$  is the total neutrino luminosity. Note that at the formation of the MNS,  $L_\nu \gtrsim 10^{53} \text{ erg s}^{-1}$  (34, 37, 38, 52), because shock heating at merger significantly increases its temperature, but  $\sim 100 \text{ ms}$  after formation,  $L_\nu$  is likely to decrease to  $\lesssim 10^{53} \text{ erg s}^{-1}$  (67). Thus, if the viscous accretion onto the MNS or the neutrino cooling has a significant effect and the MNS is marginally stable against gravitational collapse, the MNS would collapse to a BH on either of these timescales.

If the MNS mass is sufficiently low, it will not collapse to a BH in  $\sim 10 \text{ s}$ . In this case, the MNS is likely to settle into a rapidly and rigidly rotating cold NS (a so-called SMNS). The maximum mass of the SMNS depends on its rotation and can be increased by as much as  $\sim 0.4 M_\odot$  if the star is rotating rigidly at the maximum angular velocity,  $\sim \sqrt{GM_{\text{MNS}}/R^3}$  (105, 106), where  $M_{\text{MNS}}$  denotes the gravitational mass of the MNS and  $G$  is the gravitational constant. For example, if the maximum mass of a cold spherical NS is  $2.2 M_\odot$ , then the maximum mass of the SMNS would be  $\sim 2.6 M_\odot$ , so the self gravity of the SMNS could be sustained. However, because an SMNS formed in merger is magnetized, its rotational kinetic energy is subsequently dissipated through the magnetic dipole radiation if a force-free magnetic field is established outside the SMNS. If we assume that dipole magnetic radiation with luminosity  $L_B$  is present, then the spin-down timescale of the SMNS is

$$\tau_B \approx \frac{T_{\text{rot}}}{L_B} \approx 650 \text{ s} \left( \frac{B_p}{10^{15} \text{ G}} \right)^{-2} \left( \frac{M_{\text{MNS}}}{2.5 M_\odot} \right) \left( \frac{R}{15 \text{ km}} \right)^{-4} \left( \frac{\Omega}{7,000 \text{ rad s}^{-1}} \right)^{-2}, \quad 4.$$

where  $T_{\text{rot}} (\sim 0.3 M_{\text{MNS}} R^2 \Omega^2)$  is the rotational kinetic energy,  $B_p$  is the magnetic-field strength of the SMNS pole, and  $\Omega$  is the angular velocity of the SMNS. Here, we have assumed that the magnetic-field strength would be significantly enhanced at merger. This estimate shows that the rotational kinetic energy could be dissipated in  $\sim 10^3 \text{ s}$ . After the dissipation of its rotational kinetic energy, the SMNS should collapse to a BH.

## 2.2. Black Hole–Neutron Star Binaries

**Figure 2** summarizes the possible remnants and their expected evolution processes for mergers of BH-NS binaries. BH-NS binaries have two possible fates: Either the NS is tidally disrupted before it is swallowed by the BH, or it is swallowed by the BH without disruption (70). For the latter case, essentially no disk is formed and no matter is ejected, and there is no or weak EM emission.

Tidal disruption of an NS occurs if the tidal force from the BH is stronger than the self-gravity of the NS. If we assume Newtonian gravity, then we can write the condition approximately as  $GM_{\text{BH}} R_1 / r^3 > GM_{\text{NS}} / R_1^2$ . Therefore,

$$\left( \frac{GM_{\text{BH}}}{c^2 r} \right)^{3/2} \left( \frac{M_{\text{NS}}}{M_{\text{BH}}} \right) \left( \frac{R_1}{G c^{-2} M_{\text{NS}}} \right)^{3/2} > 1, \quad 5.$$

where  $r$  is the orbital separation,  $M_{\text{BH}}$  and  $M_{\text{NS}}$  are the masses of the BH and the NS, and  $R_1$  is the semimajor axis of the NS.  $R_1$  is a factor of  $\sim 1.5$  larger than the NS radius,  $R_{\text{NS}}$ , at the onset of tidal disruption. For tidal disruption, the condition of Equation 5 should be satisfied before the NS orbit

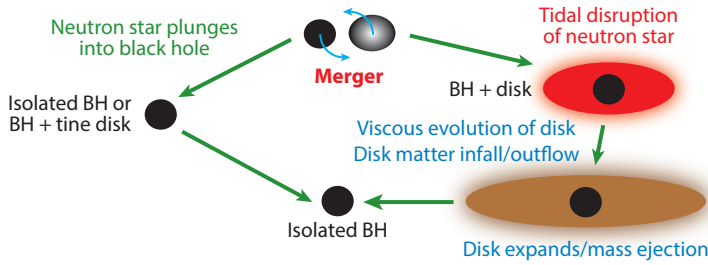


**Figure 2**

Summary of the merger and postmerger evolution of BH-NS binaries. This system has two possible fates: The NS either is or is not tidally disrupted by the companion BH. In the case of tidal disruption, the remnant is a spinning BH surrounded by a disk. The evolution process of the BH + disk system is essentially the same as that for binary NS mergers. Abbreviations: BH, black hole; NS, neutron star.

reaches the innermost stable circular orbit (ISCO) around the BH, at which  $r = \xi Gc^{-2}M_{\text{BH}}$ , where  $\xi = 6$  for nonspinning BHs and  $\xi = 1$  for extremely rapidly spinning BHs (which are corotating with the binary orbit). Here, we have assumed that  $Q = M_{\text{BH}}/M_{\text{NS}}$  is large enough that we can ignore the tidal deformation effect of NSs to the orbital motion. Then, we can rewrite Equation 5 as

$$\left(\frac{\xi}{6}\right)^{-3/2} \left(\frac{Q}{7}\right)^{-1} \left(\frac{R_1}{10Gc^{-2}M_{\text{NS}}}\right)^{3/2} > 3.25. \quad 6.$$

We note that  $Gc^{-2}M_{\text{NS}} \approx 2.0(M_{\text{NS}}/1.35M_{\odot})$  km. This condition indicates that tidal disruption occurs for low values of  $\xi$  (i.e., for rapidly spinning BHs) or for low values of  $Q$ , if the BH spin is not very large. Since the value of  $Q$  is likely to be higher than approximately four for the typical NS mass of  $1.3\text{--}1.4M_{\odot}$ , we find that a high-spin BH is needed for tidal disruption of neutron stars.

Numerical-relativity simulations have shown that for the case in which an NS is tidally disrupted, an accretion disk is subsequently formed around a spinning BH (33, 35, 36, 42, 44, 46–48, 53, 54, 107–113). Also, a fraction of neutron-rich matter is ejected from the system (see Section 3.2) (44, 53, 54, 113). The disk mass,  $M_{\text{disk}}$ , depends strongly on  $Q$ ,  $R_{\text{NS}}$ , and BH spin. Among these three parameters, the BH spin is the most substantial. For example, for a dimensionless BH spin with  $\chi = 0.75$  and  $R_{\text{NS}} \approx 13$  km,  $M_{\text{disk}}$  can be  $\sim 10\%$  and  $20\%$  of  $M_{\text{NS}}$  for  $Q = 7$  and  $3$ , respectively (113). For  $\chi = 0.9$ ,  $M_{\text{disk}}$  is  $\sim 20\%$  of  $M_{\text{NS}}$  for  $Q = 7$  and  $R_{\text{NS}} \approx 13$  km (44). Lovelace et al. (46) find that for  $\chi = 0.97$ , with  $Q = 3$  and  $R_{\text{NS}} \approx 14$  km,  $M_{\text{disk}}$  can be  $\sim 0.5M_{\text{NS}}$ .

Next, we turn our attention to MHD/viscous evolution of a disk surrounding a rapidly spinning BH after a BH-NS merger. Such an accretion disk has nearly Keplerian motion (i.e., differential rotation) and should have magnetic fields originating in the NS's magnetic field. Thus, the disk is unstable to the MRI and, as a result, is likely to be in a turbulent state (84), enhancing turbulent viscosity (102–104). Therefore, the BH accretion disk evolves through the viscous process on the timescale of Equation 2. Specifically, viscous heating and angular momentum transport, together with neutrino cooling, are the key processes. Through viscous angular momentum transport, matter in the inner part of the disk falls into the BH while its outer part gradually expands along the equatorial plane. Viscous heating increases the temperature of the disk to  $\sim 1\text{--}10$  MeV, leading to appreciable neutrino emission (66, 68, 86–91). If the density of the disk is sufficiently high ( $\gtrsim 10^{11}$  g cm $^{-3}$ ), then the optical depth to neutrinos is large enough to avoid free-streaming escape, suppressing neutrino emissivity. In this phase, the temperature of the disk is determined by the condition that the timescales of the neutrino cooling and viscous heating approximately agree with each other. Throughout the evolution of the system, the density of the

disk decreases because of the mass infall into the BH, along with expansion of the disk by viscous angular momentum transport. Then, the optical depth of the disk to neutrinos decreases (61). In this later phase, adiabatic expansion of the disk (not neutrino cooling) as well as infall into the BH become the primary cooling process, while viscous heating is always the dominant heating process. This late-phase adiabatic expansion of the disk eventually drives mass ejection (see Section 3.3).

The vicinity of spinning BHs is likely to be the site of high-energy phenomena for two reasons. First, the temperature of disks near BHs can be quite high ( $\gtrsim 10$  MeV), and hence high-energy neutrinos are copiously emitted. Because of the high temperature, the disks can be geometrically thick, so an appreciable fraction of neutrinos are emitted toward the rotational axis of the spinning BHs. This enhances the pair annihilation of neutrinos and their antineutrinos, leading to pair production of electrons and positrons, which could subsequently produce  $\gamma$ -rays through pair annihilation. If the total energy of the electrons and positrons is high enough, they could be the engine that drives an sGRB (66, 85–91).

Second, as mentioned above, the BH accretion disk is likely to be strongly magnetized due to the MRI. If the resulting magnetic pressure is high enough to blow off the matter in the vicinity of the disk, then MHD outflow could result. Subsequently, poloidal magnetic fields are likely to be formed near the spinning BH, and some of the magnetic field lines could penetrate the BH horizon. In such a magnetic-field configuration, the rotational kinetic energy of the spinning BH could be extracted by the Blandford–Znajek mechanism (92). If the extracted energy is well collimated toward the polar direction and leads to relativistic jets, an sGRB may be launched (42, 93–95).

### 3. MASS EJECTION FROM NEUTRON STAR MERGERS

During and after NS mergers, neutron-rich matter can be ejected. First, at merger, the matter is dynamically ejected on the timescale of  $\lesssim 10$  ms. Such mass ejection is referred to as dynamical mass ejection. Second, mass ejection can proceed from the merger remnant through MHD or viscous processes. Such mass ejection is referred to as the postmerger mass ejection (see **Figure 3** for these mass ejection processes). In the following subsections, we describe these two mass ejection mechanisms. We focus on the mass, velocity, and electron fraction of the ejecta because these quantities determine the property of the EM counterparts associated with the ejecta.

#### 3.1. Dynamical Mass Ejection from Binary Neutron Stars

In the mergers of binary NSs, strong shock waves are generated by the high-velocity ( $\sim 0.2c$ ) collision. In the shock waves, kinetic energy associated with the NSs' plunging motion is converted to thermal energy, which enhances thermal pressure and induces ejection of the shocked matter. Also, if an MNS is the merger remnant, it is initially highly nonaxisymmetric and oscillating. Such nonaxisymmetric MNS gravitationally exerts torque on the matter surrounding it and induces fast angular momentum transport. Through this process, the matter in the outer part of the system gains energy sufficient for ejection from the system. These two mechanisms drive dynamical mass ejection. The timescale of these processes is  $\lesssim 10$  ms. Gravitational torque causes matter to be ejected primarily in the equatorial direction, while shock heating causes it to be ejected in a less anisotropic manner.

**3.1.1. Mass.** The mass of dynamical ejecta depends on the total mass,  $m$ , and mass ratio,  $q = m_2/m_1$ , of binary NSs. For  $m > M_{\text{thr}}$ , a BH is promptly formed after the onset of merger



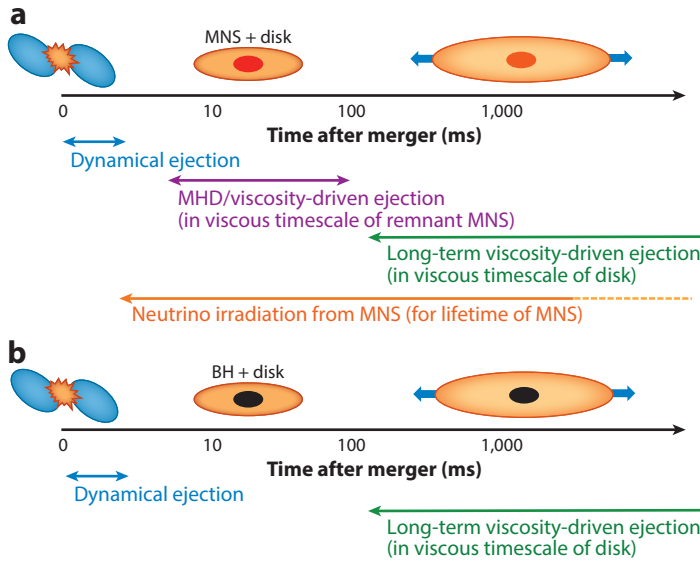


**Figure 3**

Mass ejection mechanisms during and after merger of binary NSs. Soon after the onset of merger, dynamical mass ejection occurs on the timescale of  $\lesssim 10$  ms. Subsequently, MHD- or viscosity-driven mass ejection occurs. (a) A possible mass ejection history of the formation of an MNS. Since both the MNS and the surrounding disk are differentially rotating and strongly magnetized, MHD turbulence is likely to be generated. Then, the viscous effect in the MNS can be the cause of the early viscosity-driven mass ejection  $\lesssim 100$  ms after merger. Subsequently, the viscous effect in the disk can drive mass ejection. Because of the presence of the MNS, which is a strong neutrino emitter, neutrino irradiation plays a key role in determining the electron fraction of the ejecta. (b) A possible mass ejection history of prompt BH formation, for which only dynamical mass ejection and viscosity-driven mass ejection from the disk can occur, and in which the neutrino irradiation plays a minor role. Abbreviations: BH, black hole; MHD, magnetohydrodynamic; MNS, massive neutron star; NS, neutron star.

(Figure 1). For  $q \approx 1$ ,  $\geq 99.9\%$  of the NS matter is swallowed by the formed BH (72, 73), and appreciable mass ejection cannot be expected. If the mass ratio is different from unity, a fraction of matter may be dynamically ejected (43, 55, 56). In this case, tidal torque exerted by a deformed compact object collapsing to a BH is what drives the dynamical mass ejection. Numerical-relativity simulations show that  $q \lesssim 0.8$  is necessary for dynamical mass ejection with mass  $\geq 10^{-3} M_{\odot}$ .

In the case of MNS formation, the dynamical ejecta mass depends strongly on the NS EOS as well as  $m$  for the following reason: For stiff EOSs (i.e., large NS radii), the velocity of two NSs at merger is relatively small because the minimum orbital separation is large; thus, shock heating efficiency and oscillation kinetic energy of the remnant MNS are relatively small. The result is a small dynamical ejecta mass. For practically the same reason, the dynamical ejecta mass depends on the total mass of the system, because for high total mass, the shock heating efficiency and kinetic energy of the MNS oscillation can be large, resulting in high dynamical ejecta mass. Numerical-relativity simulations show that for EOSs with  $R_{\text{NS}} \gtrsim 13$  km or for  $m \lesssim 2.6 M_{\odot}$ , the dynamical ejecta mass is of the order of  $10^{-3} M_{\odot}$  for  $q \sim 1$ . Only for  $q \lesssim 0.8$  can the dynamical ejecta mass be  $\gtrsim 0.005 M_{\odot}$  (43, 55, 56). By contrast, for  $R_{\text{NS}} \lesssim 12$  km with  $m \gtrsim 2.7 M_{\odot}$ , the dynamical ejecta mass could be  $\sim 0.01 M_{\odot}$  depending weakly on  $q$ . Thus, the dynamical ejecta mass contains information about the NS EOS.

**3.1.2. Velocity.** Since the dynamical mass ejection occurs from the vicinity of merged objects of scale  $R$ , the velocity of the ejecta should be of the order of its escape velocity, that is,  $\sim \sqrt{Gm/R} \approx 0.44c(m/2.6M_{\odot})^{1/2}(R/20\text{ km})^{-1/2}$ . Numerical-relativity simulations show that the typical average velocity is  $0.15\text{--}0.25c$  for the case of MNS formation (e.g., 43). For the prompt formation of a BH from highly asymmetric binaries, the average velocity of ejecta is higher ( $\sim 0.3c$ ) because the dynamical mass ejection proceeds only for matter in the vicinity of the object collapsing to a BH by the tidal torque exerted.

In the case of MNS formation, the dynamical mass ejection is induced in part by shock heating. For the shocked ejecta component, a fraction of matter could have a relativistic speed of up to  $\sim 0.8c$ , and the ejecta morphology is quasi-spherical (43, 45). Such high-velocity ejecta can generate a characteristic observational feature during the interaction with ISM (see Section 4.3) (58, 114).

**3.1.3. Electron fraction.** The electron fraction ( $Y_e$ ) of ejecta is a key quantity for determining the abundance of elements synthesized by r-process nucleosynthesis (15, 16, 59, 115). The abundance pattern of the r-process elements is crucial for determining the opacity of EM emission from the merger ejecta (13, 17, 18, 116, 117).

Because the typical  $Y_e$  value for NSs is quite low ( $0.05\text{--}0.1$ ),  $Y_e$  of the dynamical ejecta would also be low if the NS matter is ejected without undergoing weak-interaction processes. However, the dynamical ejecta could be influenced strongly by the weak processes. First, shock heating at merger and during subsequent evolution of the merger remnant increases the matter temperature beyond 10 MeV (34, 38). In such a high-temperature environment, electron–positron pair creation is enhanced. As a result, neutrons easily capture positrons via  $n + e^+ \rightarrow p + \bar{\nu}_e$ . Because the luminosities and average energies of electron neutrinos and electron antineutrinos are roughly equal, and because the average energies are large compared with the neutron–proton mass difference, the  $Y_e$  value of the initially neutron-rich material is driven toward  $1/2$ . Thus, in the presence of many positrons produced by pair creation, the fraction of protons and the  $Y_e$  value are increased (i.e., the neutron richness is reduced) (118).

In the presence of an MNS that is a strong neutrino emitter, the neutrino irradiation to the matter surrounding the MNS could significantly change its composition. Since neutrons and protons absorb neutrinos via  $n + \nu_e \rightarrow p + e^-$  and  $p + \bar{\nu}_e \rightarrow n + e^+$ , respectively, the fractions of neutrons and protons tend to equilibrate. Because the luminosity and average energy of electron neutrinos and electron antineutrinos from the MNS are not significantly different, the fractions of protons and neutrons approach approximately the same values (i.e.,  $Y_e$  approaches  $1/2$ , and the neutron richness is significantly reduced).

As mentioned above, there are two engines driving dynamical mass ejection: shock heating and tidal torque. Both effects play an important role in the case of MNS formation. On one hand, shock heating and neutrino irradiation from the MNS increase  $Y_e$  for a large fraction of ejecta. On the other hand, matter ejected by tidal torque does not always undergo the weak interaction: If a fraction of the matter is ejected by tidal torque without undergoing shock heating and neutrino irradiation, the low- $Y_e$  state is preserved. Therefore, the dynamical ejecta for the MNS formation case in general has components with a wide range of  $Y_e$  between  $\sim 0.05$  (i.e., the original value in NSs) and  $\sim 0.5$ , and if the weak-interaction effect is not significant, a large fraction of ejecta has low  $Y_e$  values.

In the case of prompt BH formation, most of the shock-heated matter is swallowed by the BH, and a strong neutrino irradiation source such as an MNS is absent. For asymmetric binaries, a fraction of matter is ejected by the effect of tidal torque, but in this case, the weak interaction does not play a role; therefore, the  $Y_e$  value of the ejecta is low ( $\lesssim 0.1$ ).

### 3.2. Dynamical Mass Ejection from Black Hole–Neutron Star Binaries

If an NS is tidally disrupted by its companion BH, a fraction of the NS matter is ejected. In contrast to binary NS mergers, for BH-NS binaries only the tidal effect plays an important role in the dynamical mass ejection.

Broadly speaking, the mass of dynamical ejecta is determined by how the tidal disruption of an NS proceeds. If an NS is tidally disrupted far from the ISCO of its companion BH, a fraction of the NS matter remains outside the BH horizon after merger. Numerical-relativity simulations show that for such cases, typically  $\sim 20\%$  of the matter located outside the horizon escapes from the system as ejecta (113). Thus, larger disk mass results in larger dynamical ejecta mass—up to  $\sim 0.1M_\odot$  at maximum. Of course, if NSs are not tidally disrupted, then the dynamical ejecta mass is absent. Thus, the dynamical ejecta mass ranges from 0 to  $0.1M_\odot$  for BH-NS binaries.

The average velocity of dynamical ejecta is determined by the velocity scale of the NS at tidal disruption (i.e.,  $0.2\text{--}0.3c$ ). Again, high-velocity matter can be present because a part of the ejecta comes from the vicinity of the BH horizon. In particular, in the case of a spinning BH, the radius of the event horizon is small, so the fraction of the high-velocity component can be increased.

Because dynamical ejecta is launched predominantly by tidal torque, and weak-interaction processes such as neutrino irradiation play minor roles in the ejecta, the  $Y_e$  value of the dynamical ejecta is always low ( $\lesssim 0.1$ ) (36, 48, 54). This result differs significantly from that in binary NS mergers resulting in an MNS (see Section 3.1).

### 3.3. Viscosity-Driven Mass Ejection from Merger Remnants

In general, after merger of NS binaries, an MNS or a BH surrounded by a disk is formed. At their formation, both the MNS and the disk are differentially rotating and likely to be strongly magnetized; therefore, MHD turbulence should be induced. Turbulent viscosity could then be strongly enhanced, as mentioned in Section 2. This viscous effect induces the so-called viscosity-driven mass ejection (61, 62, 65, 67). We describe this mechanism in the following subsections.

**3.3.1. Mass ejection driven by the viscous effect of massive neutron stars.** First, we discuss the case of MNS formation for binary NS mergers. If MHD turbulence develops and the resulting turbulent viscosity is sufficiently high, the differential rotation energy of the remnant MNS could be the energy source of mass ejection. The angular momentum is transported in the MNS on the timescale described by Equation 1. As a result, the angular velocity profile of the MNS is rearranged into a rigidly rotating state. The density and pressure profiles also change during this transition because the centrifugal force is rearranged. Here, the total rotational kinetic energy of an MNS estimated by  $T_{\text{kin}} \sim I\Omega^2/2 \sim 0.3M_{\text{MNS}}R^2\Omega^2$  (105, 106) is quite large:

$$T_{\text{kin}} \sim 2 \times 10^{53} \left( \frac{M_{\text{MNS}}}{2.6M_\odot} \right) \left( \frac{R}{15 \text{ km}} \right)^2 \left( \frac{\Omega}{7,000 \text{ rad s}^{-1}} \right)^2 \text{ erg.} \quad 7.$$

This energy could be redistributed in the viscous timescale of  $\sim 10\text{--}20$  ms. In association with the change in density profile, strong density waves are generated. These density waves subsequently propagate outward, and consequently, shocks are generated in the disk. The shock waves sweep matter into the disk and envelope, which subsequently undergoes outgoing motion. If the energy of a fraction of the matter becomes high enough, mass ejection could occur.

Because the power of the density waves depends on the strength of the viscous effect, the ejecta mass in this process depends on the  $\alpha$  parameter. A numerical-relativity simulation has shown that the ejecta mass is  $\sim 0.01M_\odot(\alpha_{\text{vis}}/0.02)$  (67). The ejecta is launched originally from the vicinity of

the MNS. Therefore, the typical velocity of this ejecta component agrees approximately with the escape velocity of the MNS (i.e.,  $\sim 0.15c$ ). The  $Y_e$  of this component is widely distributed, as in dynamical ejecta. However, the low- $Y_e$  components are absent because the neutrino irradiation from the MNS is strong enough to drive  $Y_e$  values above 0.2, yielding values between 0.2 and 0.5.

**3.3.2. Mass ejection driven by the viscous effect of disks.** For the longer-term evolution, viscous heating and angular momentum transport in the disk play important roles in mass ejection regardless of the formation of MNS or BH. In early disk evolution, thermal energy generated by viscous heating is consumed primarily by neutrino emission. This stage is described by a neutrino-dominated accretion disk (87) with a fraction of the outflow in the polar direction driven by neutrino heating, including neutrino–antineutrino pair-annihilation heating. In the later stages, the mass, density, and temperature of the disk decrease because of the outflow and accretion onto the MNS. The decrease of the temperature,  $T$ , causes a reduction in the neutrino emissivity because of its strong dependence on  $T$ , which is approximately proportional to  $T^6$  (86). Then, the viscous heating is used primarily for the adiabatic expansion of the disk in the equatorial direction. The continuous viscous heating causes the disk matter to eventually escape from the system as ejecta.

Because viscous mass ejection from a disk should occur regardless of the viscous parameter (for reasonably large values of  $\alpha_{\text{vis}}$ ), the ejecta mass in this process depends weakly on its value. Numerical simulations show that the ejecta mass could be a substantial fraction (more than half) of the disk mass of  $0.01\text{--}0.1M_\odot$  for the presence of an MNS (62, 63, 67). For the presence of a BH, the mass falling into the BH is larger than that of the outflow. However, numerical simulations for disks around spinning BHs show that  $\sim 20\%$  of the disk mass can be ejected (61, 65). If the matter is efficiently ejected by MHD processes, this fraction may be increased by a factor of two (66, 68).

The ejecta in this mechanism is launched primarily from the outer part of disks. If the mass ejection occurs at a radius of  $r \gtrsim 100Gc^{-2}M$  ( $M = M_{\text{MNS}}$  or  $M_{\text{BH}}$ ), then the characteristic velocity would be  $\lesssim 0.1c$ . Thus, the typical velocity of this ejecta component is smaller than that of dynamical ejecta and early viscosity-driven ejecta powered by the MNS.

The values of  $Y_e$  within the dynamical ejecta vary widely. However, the low end depends strongly on the presence or absence of the MNS, which can be the source of strong neutrino irradiation (62). In the presence of the MNS, the low end of  $Y_e$  could be  $\sim 0.3$  (63, 67), whereas in its absence (i.e., in the presence of a BH), low  $Y_e$  values are preserved for a substantial fraction of the ejecta (62, 65). The reasons are that the disk is dense and electrons are degenerate, resulting in the low- $Y_e$  state in the disk, and that the weak interaction does not play an important role because neutrino irradiation is weak in this case (61).

### 3.4. Summary of Ejecta

**Table 1** summarizes the typical properties of ejecta, showing that the ejecta quantities depend strongly on the binary parameters, so that the observational features of the EM emission (especially kilonova emission; see Section 4.2) can be different for each merger event.

## 4. ELECTROMAGNETIC COUNTERPARTS OF NEUTRON STAR MERGERS

NS mergers eject a substantial amount of neutron-rich material, in which r-process nucleosynthesis is robust. Subsequently, synthesized radioactive elements shine, in particular, as a kilonova

**Table 1** Typical properties of ejecta<sup>a</sup>

Type of binary	Remnant	$M_{\text{ej,dyn}}$	$M_{\text{ej,vis}}$	$Y_{e,\text{dyn}}$	$Y_{e,\text{vis}}$	$\langle v_{\text{ej}} \rangle$
Low- $m$ BNS	SMNS	$O(10^{-3})$	$O(10^{-2})$	0.05–0.5	0.3–0.5	0.15
Mid- $m$ BNS (stiff EOS)	HMNS	$O(10^{-3})$	$O(10^{-2})$	0.05–0.5	0.2–0.5	0.15
Mid- $m$ BNS (soft EOS)	HMNS	$\sim 10^{-2}$	$O(10^{-2})$	0.05–0.5	0.2–0.5	0.20
High- $m$ BNS ( $q \sim 1$ )	BH	$< 10^{-3}$	$< 10^{-3}$	ND	ND	ND
High- $m$ BNS ( $q \ll 1$ )	BH	$O(10^{-3})$	$\lesssim 10^{-2}$	0.05–0.1	0.05–0.3	0.30
BH-NS	BH	0–0.1	0–0.1	0.05–0.1	0.05–0.3	0.30

<sup>a</sup>Low- $m$ , mid- $m$ , or high- $m$  implies that the remnant soon after the merger is an SMNS, HMNS, or BH.  $M_{\text{ej,dyn}}$  and  $M_{\text{ej,vis}}$  are the dynamical and postmerger ejecta mass in units of  $M_{\odot}$ ;  $\langle v_{\text{ej}} \rangle$  is the average velocity of the dynamical ejecta in units of  $c$ ;  $Y_{e,\text{dyn}}$  is the  $Y_e$  of the dynamical ejecta; and  $Y_{e,\text{vis}}$  is the  $Y_e$  of the postmerger ejecta.

Abbreviations: BH, black hole; BNS, binary neutron star; EOS, equation of state; HMNS, hypermassive neutron star; ND, not determined; SMNS, supramassive neutron star.

(macronova). In addition, the ejecta have high kinetic energy with mildly relativistic velocities, leading to a long-lasting synchrotron remnant. In the following subsections, we first summarize the general properties of r-process nucleosynthesis in mergers, then describe models of kilonovae and synchrotron remnants as promising EM signals.

#### 4.1. r-Process Nucleosynthesis and Ejecta Opacity

As described in Section 3, above, dense neutron-rich matter is generally ejected in NS mergers. The neutron-rich ejecta can subsequently synthesize heavy elements through r-process nucleosynthesis, that is, by rapid neutron capture, where the capture timescale is typically shorter than the  $\beta$  decay timescales (118).

In the r-process nucleosynthesis, the abundance of elements synthesized depends primarily on neutron richness, entropy, and density (118). Among these properties, the neutron richness (i.e.,  $Y_e$ ) is the key quantity in mergers. Numerical calculations show (15, 16) that for ejecta with neutron-rich matter of  $Y_e \lesssim 0.1$ , r-process elements with mass number  $A \gtrsim 120$  (i.e., the elements in the so-called second and third peaks) are robustly synthesized. In this case, the mass fraction of elements with  $A \lesssim 120$  is quite small. This finding implies that for BH-NS mergers and binary NS mergers collapsing promptly to a BH, predominantly heavy r-process elements are synthesized. By contrast, from ejecta with  $Y_e \gtrsim 0.25$ , heavy elements with  $A \gtrsim 130$  (e.g., lanthanide) are not synthesized (16, 59, 115). In the presence of a wide range of  $Y_e$  values in ejecta, r-process elements with a large mass range are synthesized, as was first pointed out in Reference 59. As mentioned in Section 3, for mergers of binary NSs leading to an MNS, matter with a wide range of  $Y_e$  values (0.05–0.5; see Table 1) is ejected; thus, r-process elements with  $A \gtrsim 70$  are synthesized simultaneously.

#### 4.2. Kilonovae (Macronovae)

Kilonovae are UV–optical–IR transients powered radioactively by r-process elements freshly synthesized in merger ejecta.

**4.2.1. Radioactive heating.** The radioactive decay channels of neutron-rich heavy elements are (a)  $\beta$  decay, (b)  $\alpha$  decay, and (c) fission. The specific heating rate of the second and third of these channels depends sensitively on the abundance of superheavy nuclei ( $A \geq 210$  for  $\alpha$  decay and  $A \geq 250$  for fission). In the following subsections, we describe the heating process for each channel.

**4.2.1.1.  $\beta$  decay.**  $\beta$ -unstable nuclei decay toward the stability valley without changing their atomic mass number. Because the number of nuclei is conserved for each atomic mass number, the decay rate is approximately proportional to  $t^{-1}$ , where radioactive species with mean lifetimes  $\tau \sim t$  contribute predominantly to the decay rate at  $t$ . The electron energy liberated in each decay generally decreases with lifetime as  $E_e \propto \tau^{-1/5}$  to  $\tau^{-1/3}$ . Thus, the energy-releasing rate in  $\beta$  decay electrons per unit mass is  $\dot{q}_e(t) \propto t^{-6/5}$  to  $t^{-4/3}$  (13, 119), which is typically written as

$$\dot{q}_e(t) \approx 3 \cdot 10^9 \text{ erg s}^{-1} \text{ g}^{-1} \left( \frac{t}{1 \text{ day}} \right)^{-4/3}. \quad 8.$$

$\beta$  decay is often followed by  $\gamma$ -ray emission, and the efficiency of the energy release in  $\gamma$ -rays is  $\sim 0.3$ – $2$  times that of  $\dot{q}_e(t)$ .  $\beta$  decay and  $\gamma$ -ray emission are the primary heating sources of kilonovae.

**4.2.1.2.  $\alpha$  decay.** Neutron-rich elements with  $210 \leq A \lesssim 254$  increase their proton fraction through  $\beta$  decay until the point at which they are predominantly disintegrated by  $\alpha$  decay. After a number of  $\alpha$  decays and  $\beta$  decays, they eventually reach stable nuclei with  $A < 210$ . Each  $\alpha$  decay liberates energy of  $\sim 5$ – $10$  MeV. Among the  $\alpha$ -unstable elements,  $^{222}\text{Rn}$ ,  $^{223}\text{Ra}$ ,  $^{224}\text{Ra}$ ,  $^{225}\text{Ra}$ , and  $^{225}\text{Ac}$  are particularly relevant for the kilonova heating rate (120). In a decay chain of these elements, a total of 20–30 MeV of energy is released. Nuclei with  $222 \leq A \leq 225$  can dominate over  $\beta$  decay heating for times longer than a few days, if the total mass of these elements is  $\gtrsim 10^{-3} M_\odot$  (Figure 4).

**4.2.1.3. Spontaneous fission.** Transuranium nuclides with  $A \gtrsim 240$  may be disintegrated by spontaneous fission, in which  $\sim 100$ – $200$  MeV of energy is released as kinetic energy of fission

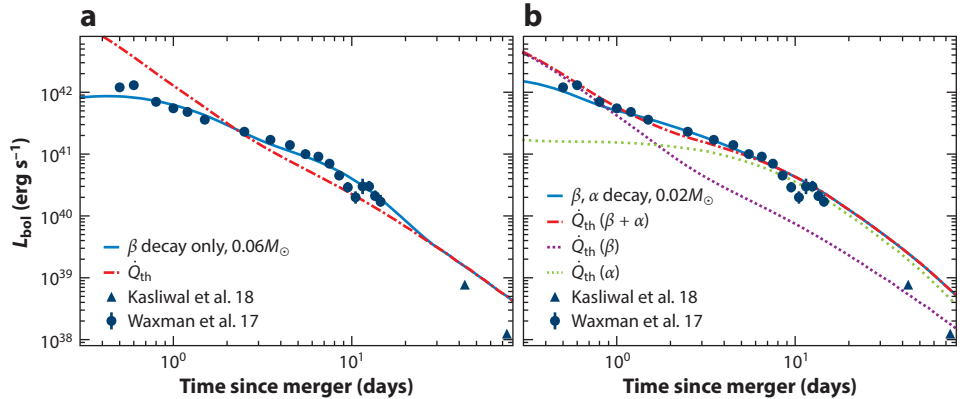


**Figure 4**

$\beta$  decay heating rate and bolometric light curve models for (a) ejecta of the solar r-process abundance with  $A \geq 85$  and (b) those including  $\alpha$  decay heating. In panel a, the total r-process mass and the typical ejecta velocity are set to  $0.06 M_\odot$  and  $0.15c$ . The opacity is assumed to be  $1 \text{ cm}^2 \text{ g}^{-1}$  for  $v > 0.15c$  and  $7 \text{ cm}^2 \text{ g}^{-1}$  for  $v \leq 0.15c$ . Note that this opacity distribution is phenomenological to fit the bolometric data and is somewhat motivated by the models presented in References 129 and 130. In panel b, the initial abundances of  $A = 222$ , 223, 224, and 225 are taken to be  $Y_A = 4.0 \times 10^{-5}$ ,  $2.7 \times 10^{-5}$ ,  $4.1 \times 10^{-5}$ , and  $2.7 \times 10^{-5}$ , respectively, corresponding to the DZ31 model presented in Reference 120. In this case, the total r-process mass and the typical ejecta velocity are  $0.02 M_\odot$  and  $0.1c$ . The opacity is assumed to be  $0.1 \text{ cm}^2 \text{ g}^{-1}$  for  $v > 0.1c$  and  $1 \text{ cm}^2 \text{ g}^{-1}$  for  $v \leq 0.1c$ . Also depicted are the observed bolometric light curve data of GW170817 (125) and  $\nu L_\nu$  of the late-time Spitzer observations at  $4.5 \mu\text{m}$  (133).

fragments. Thus, the energy release of each fission is greater by a factor of  $\gtrsim 100$  than in  $\beta$  decay. Although the  $Q$  value and half-life of spontaneous fission, as well as the abundance of transuranium nuclides synthesized in merger ejecta, are highly uncertain, spontaneous fission could potentially dominate the heating rate at later times of  $\gtrsim 10$  days (59, 120–122). For instance, a notable element is  $^{254}\text{Cf}$ , of which the half-life is 60.5 days and the  $Q$  value is 185 MeV (120, 122).

High-energy charged particles (electrons,  $\alpha$  particles, and fission fragments) produced by radioactive decay deposit their kinetic energy into the thermal energy of merger ejecta on the following timescale (123, 124):

$$t_{\text{th}} \approx \left( \frac{\sigma_{\text{st}}(E_i) N v_i}{E_i} \right)^{-1}, \quad 9.$$

where  $\sigma_{\text{st}}$  is the stopping power determined predominantly by the collisional ionization and excitation of ions,  $N$  is the number density of ions, and  $E_i$  and  $v_i$  are the initial kinetic energy and velocity of a particle, respectively.  $E_i$  is typically 0.1–1 MeV for electrons, 5 MeV for  $\alpha$  particles, and 100 MeV for fission fragments. Since density decreases with time in expanding ejecta, the thermalization time increases and eventually exceeds the expansion time.

The thermalization timescales for  $\beta$ ,  $\alpha$ , and  $\gamma$  decay are

$$t_{\text{th},\beta} \sim 30 \text{ days} \left( \frac{M_{\text{ej}}}{0.05 M_{\odot}} \right)^{1/2} \left( \frac{v_{\text{ej}}}{0.1c} \right)^{-3/2} \left( \frac{E_i}{0.5 \text{ MeV}} \right)^{-1/2}, \quad 10.$$

$$t_{\text{th},\alpha} \sim 45 \text{ days} \left( \frac{M_{\text{ej}}}{0.05 M_{\odot}} \right)^{1/2} \left( \frac{v_{\text{ej}}}{0.1c} \right)^{-3/2} \left( \frac{E_i}{5 \text{ MeV}} \right)^{-1/2}, \quad 11.$$

$$t_{\text{th},\gamma} \sim 2.4 \text{ days} \left( \frac{\kappa_{\gamma}}{0.05 \text{ cm}^2 \text{ g}^{-1}} \right)^{-1} \left( \frac{M_{\text{ej}}}{0.05 M_{\odot}} \right)^{1/2} \left( \frac{v_{\text{ej}}}{0.1c} \right)^{-1}, \quad 12.$$

where  $M_{\text{ej}}$  and  $v_{\text{ej}}$  denote the mass and typical velocity of the ejecta, and  $\kappa_{\gamma} \approx 0.05 \text{ cm}^2 \text{ g}^{-1}$  is the mass absorption coefficient of r-process elements at a  $\gamma$ -ray energy of  $\sim 1$  MeV. Note that the thermalization time for fission fragments is  $\sim 2t_{\text{th},\alpha}$  (123).

Once  $t > t_{\text{th},a}$  (where  $a = \alpha, \beta, \gamma$ , or spontaneous fission) is achieved, the thermalization rate becomes lower than the adiabatic cooling rate; therefore, a significant fraction of the radioactive energy is lost adiabatically for charged particles and the  $\gamma$ -ray heating rate declines exponentially. The heating rate is equal to the energy generation rate for  $t \ll t_{\text{th},a}$ , whereas for  $t \gtrsim t_{\text{th},a}$  the heating rate deviates from the energy generation rate (124, 125) and goes approximately as  $\propto t^{-3}$  for  $t \gg t_{\text{th},a}$  (125).

**4.2.2. Opacity.** The opacity of photons plays an essential role in the light curves and spectra of kilonovae. In kilonovae, opacity is determined primarily by the bound–bound absorption of heavy elements (18, 126). Notably, the bound–bound absorption opacity of open  $f$ -shell elements (lanthanides and actinides) differs significantly from the opacity of others, because open  $f$ -shell elements have such a high number of excited levels with a relatively low excitation energy that the number of transition lines in the optical and IR bands is greatly enhanced (17, 18, 126). Radiation transfer simulations of merger ejecta show that the mean opacity,  $\kappa$ , is  $\gtrsim 10 \text{ cm}^2 \text{ g}^{-1}$  for lanthanide-rich ejecta, versus  $\sim 0.1 \text{ cm}^2 \text{ g}^{-1}$  for lanthanide-free ejecta (17, 18, 116, 126–128). This finding implies that the  $Y_e$  distribution of ejecta, which primarily determines the abundance pattern of r-process elements, is key for determining the features of kilonovae.



**4.2.3. Typical light curve.** For merger ejecta, the light curve peaks on the following timescale (13):

$$t_p \approx \sqrt{\frac{\kappa M_{\text{ej}}}{4\pi c v_{\text{ej}}}} \approx 10 \text{ days} \left( \frac{\kappa}{10 \text{ cm}^2 \text{ g}^{-1}} \right)^{1/2} \left( \frac{M_{\text{ej}}}{0.04 M_{\odot}} \right)^{1/2} \left( \frac{v_{\text{ej}}}{0.1c} \right)^{-1/2}. \quad 13.$$

The luminosity and effective temperature are estimated as

$$L_{\text{bol}}(t_p) \approx \dot{Q}_{\text{th}}(t_p) = M_{\text{ej}} \cdot \dot{q}_{\text{th}}(t_p) \approx 4 \cdot 10^{40} \text{ erg s}^{-1} \left( \frac{t_p}{10 \text{ days}} \right)^{-1.3} \left( \frac{M_{\text{ej}}}{0.04 M_{\odot}} \right), \quad 14.$$

$$T_{\text{eff}}(t_p) \approx \left( \frac{L_{\text{bol}}(t_p)}{4\pi \sigma v_{\text{ej}}^2 t_p^2} \right)^{1/4} \approx 2,000 \text{ K} \left( \frac{L_{\text{bol,p}}}{4 \cdot 10^{40} \text{ erg s}^{-1}} \right)^{1/4} \left( \frac{v_{\text{ej}}}{0.1c} \right)^{-1/2} \left( \frac{t_p}{10 \text{ days}} \right)^{-1/2}, \quad 15.$$

where  $\sigma$  is the Stefan–Boltzmann constant. These equations show that lanthanide-free ejecta are brighter and bluer and peak earlier than lanthanide-rich ejecta if the mass, velocity, and specific heating rate are the same.

**Figure 4a** shows the  $\beta$  decay heating rate for the solar r-process abundance pattern with  $A \geq 85$  and a bolometric light curve calculated using a simple one-dimensional ejecta model, in which  $\kappa$  is assumed to be  $1 \text{ cm}^2 \text{ g}^{-1}$  for  $v > 0.15c$  and  $7 \text{ cm}^2 \text{ g}^{-1}$  for  $v \leq 0.15c$  with  $M_{\text{ej}} = 0.06 M_{\odot}$ . Note that this opacity distribution is adjusted phenomenologically to fit the bolometric data and is somewhat motivated by the models presented in, for instance, References 129 and 130. Kilonova bolometric light curves have the following generic features. The bolometric luminosity is lower than the heating rate in the early phase, in which most of the ejecta is optically thick. When the optical depth falls below  $\sim c/v_{\text{ej}}$ , photons in the entire ejecta begin to diffuse out from the ejecta without significant adiabatic losses. At later times, the ejecta density becomes so low that most of photons in the ejecta diffuse out within one dynamical time; then, the bolometric luminosity approaches approximately the total heating rate.

**Figure 4b** illustrates the case in which  $\alpha$  decay enhances the kilonova heating rate. In the example shown in the figure, the  $\alpha$  decay heating rate of the DZ31 model presented in Reference 120 is added to the  $\beta$  decay heating rate. Note that this model predicts the production of much larger amounts of  $\alpha$ -unstable nuclei than other nuclear mass models (120). With this model, the ejecta mass of  $\sim 0.02 M_{\odot}$  is sufficient to generate bolometric light curve as bright as the light curve with only  $\beta$  decay and  $M_{\text{ej}} \approx 0.06 M_{\odot}$ .

### 4.3. Synchrotron Emission

The interaction of merger ejecta with the surrounding ISM produces a long-lasting synchrotron emission observable in multiwavelength bands from radio to X-rays (30). Various types of merger ejecta, including dynamical and postmerger ejecta, sGRB jets, and cocoons, can produce such signals. Here, we focus on the signal arising from the dynamical ejecta because it is closely related to the merger dynamics (114, 131).

We estimate the flux from dynamical ejecta by modeling it as a spherical expanding shell with a single velocity and neglecting relativistic corrections. An ejecta with kinetic energy,  $E$ , and initial velocity in units of  $c$ ,  $\beta_i$ , expanding in the surrounding ISM of a constant number density,  $n$ , is



decelerated on the following timescale:

$$t_{\text{dec}} \approx 30 \text{ days} \left( \frac{E}{10^{49} \text{ erg}} \right)^{1/3} \left( \frac{n}{1 \text{ cm}^{-3}} \right)^{-1/3} \beta_i^{-5/3}. \quad 16.$$

The ejecta velocity (in units of  $c$ ),  $\beta$ , is constant for  $t < t_{\text{dec}}$  and decreases as  $\propto t^{-3/5}$  for  $t \gtrsim t_{\text{dec}}$  during the adiabatic expansion phase. The light curve has a peak at  $t \sim t_{\text{dec}}$ .<sup>1</sup>

$$F_{\nu, \text{peak}} \approx 3 \text{ mJy} \left( \frac{E}{10^{49} \text{ erg}} \right) \left( \frac{n}{1 \text{ cm}^{-3}} \right)^{(p+1)/4} \left( \frac{\epsilon_B}{0.1} \right)^{(p+1)/4} \left( \frac{\epsilon_e}{0.1} \right)^{p-1} \beta_i^{(5p-7)/2} \\ \times \left( \frac{D}{100 \text{ Mpc}} \right)^{-2} \left( \frac{\nu}{1.4 \text{ GHz}} \right)^{-(p-1)/2}, \quad 17.$$

where  $\epsilon_B$  and  $\epsilon_e$  are the conversion efficiencies of internal energy of the shocked ISM to magnetic-field energy and accelerated electron energy, respectively, and  $p$  is the power-law index for the distribution function of accelerated electrons. The value of  $p$  is likely to be two to three, as inferred from the GRB afterglow and radio-supernova observations. Notably, the peak flux is quite sensitive to the ejecta velocity. For a given ejecta mass, the flux increases with velocity as  $\propto \beta^{4.75}$  for  $p = 2.5$ ; therefore, the detection of such signals would prove the velocity profile of merger ejecta.

The above estimate is valid if the following three conditions are satisfied: (a) The self-absorption is negligible ( $\nu > \nu_a$ ), (b) the observed frequency is above the characteristic synchrotron frequency ( $\nu > \nu_m$ ), and (c) the observed frequency is below the synchrotron cooling frequency ( $\nu < \nu_c$ ). Here, the characteristic synchrotron frequency and the cooling frequency are given, respectively, by

$$\nu_m \approx 1 \text{ GHz} \left( \frac{n}{1 \text{ cm}^{-3}} \right)^{1/2} \left( \frac{\epsilon_B}{0.1} \right)^{1/2} \left( \frac{\epsilon_e}{0.1} \right)^2 \beta^5, \quad 18.$$

$$\nu_c \approx 10^{14} \text{ Hz} \left( \frac{n}{1 \text{ cm}^{-3}} \right)^{-3/2} \left( \frac{\epsilon_B}{0.1} \right)^{-3/2} \left( \frac{t}{30 \text{ days}} \right)^{-2} \beta^{-3}, \quad 19.$$

and the self-absorption frequency at  $t_{\text{dec}}$  is estimated to be

$$\nu_{a, \text{dec}} \approx 1 \text{ GHz} \left( \frac{E}{10^{49} \text{ erg}} \right)^{\frac{2}{3(p+4)}} \left( \frac{n}{1 \text{ cm}^{-3}} \right)^{\frac{3p+14}{6(p+4)}} \left( \frac{\epsilon_B}{0.1} \right)^{\frac{p+2}{2(p+4)}} \left( \frac{\epsilon_e}{0.1} \right)^{\frac{2(p-1)}{p+4}} \beta_0^{\frac{15p-10}{3(p+4)}}. \quad 20.$$

The above equations show that  $\nu_m$  and  $\nu_a$  are typically lower than the radio frequency for subrelativistic ejecta with  $n \lesssim 1 \text{ cm}^{-3}$  and that the cooling break is expected to occur between the optical and X-ray bands.

As discussed in Section 3.1.2, above, the velocity of dynamical ejecta is typically  $\sim 0.2c$  and can reach up to  $\sim 0.8c$ . The total kinetic energy is  $\sim 10^{50} - 10^{51} \text{ erg}$ , and the kinetic energy in the fast component with  $v \gtrsim 0.7c$  is  $\sim 10^{47} - 10^{49} \text{ erg}$ , depending on the mass of the binary and NS EOS (**Figure 5**) (58, 114). Such a velocity distribution results in a relatively flat and years-long afterglow light curve.

<sup>1</sup>The peak time is longer than  $t_{\text{dec}}$  when the synchrotron self-absorption is important. Such a delay of the peak can occur for mergers at high ISM densities ( $\gtrsim 1 \text{ cm}^{-3}$ ) and/or low observed frequencies ( $\lesssim 1 \text{ GHz}$ ).

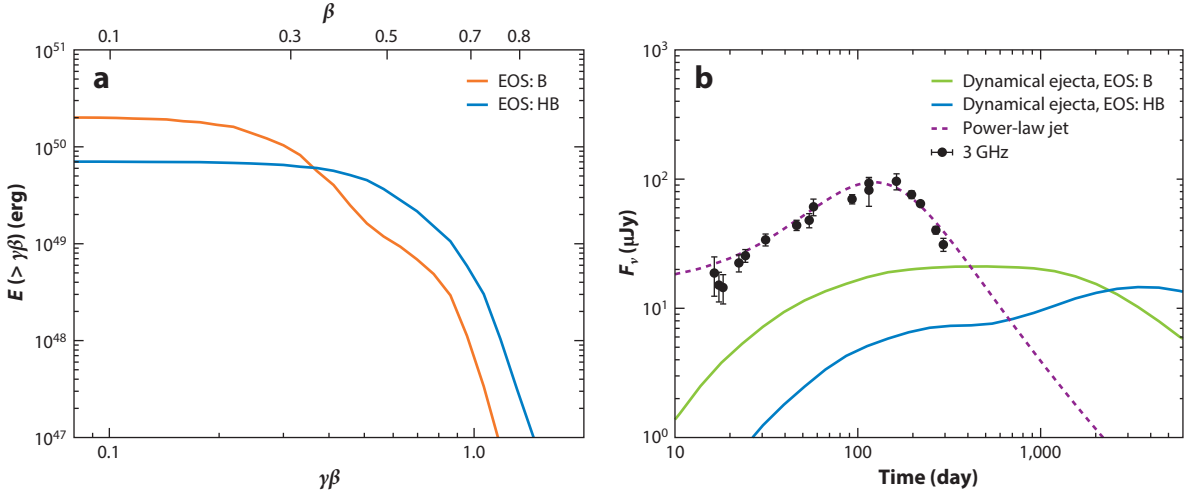


**Figure 5**

Kinetic energy of dynamical ejecta as a function of four (a) velocity and (b) afterglow light curves. The results of dynamical ejecta from binary neutron star mergers with two different EOSs (B and HB) and with mass  $m_1 = m_2 = 1.35M_\odot$  are shown. To compute these light curves, we employ  $n = 10^{-3} \text{ cm}^{-3}$  and microphysics parameters of  $\epsilon_B = \epsilon_e = 0.1$  and  $p = 2.2$  (114). Also depicted are the observed data of the afterglow in GW170817 at 3 GHz and a light curve for a power-law structured jet model, which agrees with the light curve data (142) and the observed superluminal motion (144). Abbreviation: EOS, equation of state.

## 5. GW170817

Observations of EM counterparts to GW170817 have, for the first time, provided valuable information to test theoretical predictions for mass ejection and associated EM emission. In this section, we summarize the observational features of the EM counterparts and briefly describe theoretical models that are broadly consistent with the observational results.

### 5.1. Kilonova Observation

**Figure 4** shows the observed bolometric light curve data of GW170817 (23, 24, 26, 125, 132) and  $\nu L_\nu$  of the late-time Spitzer observations at  $4.5 \mu\text{m}$  (133). Here, the late-time Spitzer data are considered approximately as the bolometric luminosity. The observed data are largely consistent with  $\beta$  decay heating with  $M_{\text{ej}} = 0.06M_\odot$ . Two notable features of this kilonova are that the light curve peaks at  $\lesssim 0.5$  days and that the peak luminosity reaches  $\sim 10^{42} \text{ erg s}^{-1}$ . As shown by Equation 13, this fact requires that some fractions of the ejecta have a low opacity ( $\lesssim 1 \text{ cm}^2 \text{ g}^{-1}$ ), suggesting that there exists a substantial amount of material with a very low or even no lanthanide fraction. By contrast, the evolution of the temperature (spectrum) at later times indicates the existence of a lanthanide-rich component. Therefore, the kilonova in GW170817 presents evidence that merger ejecta has components with a broad range of  $Y_e$  values (e.g., **Figure 6**).

As discussed in Section 3.1.3, dynamical ejecta has a wide range of  $Y_e$  values, but numerical-relativity simulations show that the dynamical ejecta mass would be  $\lesssim 10^{-2}M_\odot$ , which is smaller by a factor of two or more than that required to reproduce the observed luminosity. This suggests that the merger remnant would eject  $\gtrsim 0.03M_\odot$  from the remnant MNS and/or accretion disk (see Section 3). The origin of the different  $Y_e$  components and how they are spatially distributed are under debate. Several models suggested to date are as follows.

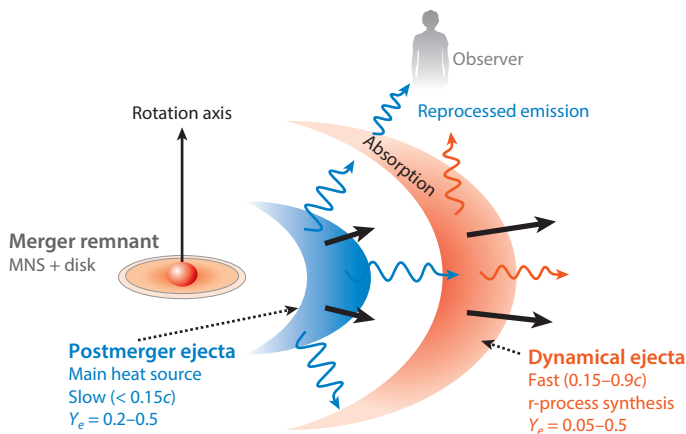


**Figure 6**

Schematic picture of the ejecta profile for the case in which a long-lived MNS is formed as a remnant. The outer falcate component denotes the neutron-rich dynamical ejecta. The inner falcate component denotes the less neutron-rich postmerger ejecta, which is slower than the dynamical ejecta. Note that the gravitational-wave observation indicates that the merger remnant of GW170817 is seen along the direction  $\theta \lesssim 30^\circ$  from the rotation axis. Abbreviation: MNS, massive neutron star.

1. Angular structure model. A lanthanide-free (blue) component and a lanthanide-rich (red) one are angularly separated; for instance, the polar ejecta is lanthanide free (134). Fitting the photometric light curve data of GW170817 leads to mass  $\sim 0.01M_\odot$  and velocity  $0.3c$  for the blue component and mass  $\sim 0.04M_\odot$  and velocity  $0.1c$  for the red component (23). Introducing another component results in a better fit to the data (129).
2. Radial structure mode. The composition (opacity) varies with the ejecta velocity; for example, the opacity of the fast-moving (slow-moving) material is  $0.8$  ( $5$ )  $\text{cm}^2 \text{g}^{-1}$ , when the two components are separated at  $v = 0.1c$  (26, 130).
3. Temporal variation model. The opacity evolves with time, which is expected from the time variation of the temperature and density of the ejecta (125). The form  $\kappa = \kappa_M(t/t_M)^\gamma$  is applied to GW170817, and  $\kappa_M \approx 0.3 \text{ cm}^2 \text{g}^{-1}$ ,  $\gamma \approx 0.6$ , and  $t_M \approx 1$  day.
4. Model motivated by numerical relativity. This model employs two (or three) ejecta components motivated by the results of numerical-relativity simulations for merger and postmerger (135–137). On the basis of the numerical results, the composition is varied both radially and angularly, and nontrivial radiation transfer effects are taken into account.

**Figure 7** compares optical and near-IR light curves of the kilonova associated with GW170817 and theoretical curves derived by a radiation-transfer simulation in the background of an ejecta model obtained from numerical-relativity simulations (see **Figure 6** for a schematic). The figure illustrates that this model works well (137). However, it is not yet clear whether every kilonova agrees with the prediction of numerical relativity, and comparison with a number of future events is clearly needed to establish the standard picture for kilonovae.

Before closing this section, we note that  $\alpha$  decay and spontaneous fission can potentially enhance the heating rate at late times (see **Figure 4** for  $\alpha$  decay). Although we cannot conclude whether or not such heavy elements play a role in the EM emission of GW170817, the estimated ejecta mass is significantly reduced from  $\sim 0.05M_\odot$  if these decay channels are important. In future events, it may be possible to identify a signature of heavy elements using a bolometric light curve at late times  $\gg 10$  days.

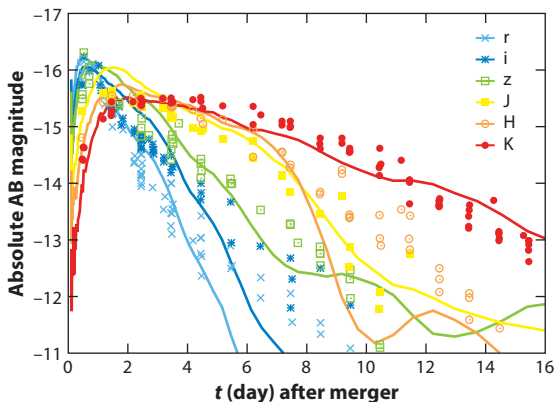


**Figure 7**

Optical and near-IR light curves (r, i, z, J, H, and K bands) of the kilonova associated with GW170817 (points) and theoretical model light curves (lines) based on numerical-relativity simulations (see **Figure 6**), assuming a viewing angle of  $\sim 25^\circ$  (137). All of the magnitudes are given in AB magnitudes. The optical and near-IR data points are from Reference 129.

## 5.2. Synchrotron Emission and Jet

The X-ray and radio afterglows of GW170817 were discovered 9 and 16 days after the merger, respectively (138, 139). The light curves rise as  $\propto t^{0.8}$  until  $\sim 150$  days (140), after which both X-ray and radio light curves fall quickly as  $\propto t^{-2.2}$  (141, 142). The spectrum of the afterglow is consistent with a single power law,  $F_\nu \propto \nu^{-0.6}$ , from the radio to X-ray bands (143), which is described well by synchrotron radiation emitted by accelerated electrons in the shocked ISM. The slow rise over a timescale of 150 days is attributed to the fact that the jet structure includes a cocoon component, and this feature is quite different from the typical GRB afterglow light curve. It is also remarkable that the fast decline of the light curve agrees with the light curve predicted for the postjet break regime of collimated jet models. Furthermore, very long baseline interferometry observations reveal that the unresolved radio-emitting region exhibits a superluminal motion with a Lorentz factor of approximately four (144). These observational features confirm that the afterglow arises from a narrowly collimated relativistic jet with some structure observed from off-axis. The kinetic energy and jet-half opening angle are estimated as  $E_j \approx 10^{49}$ – $10^{50}$  erg and  $\theta_j \lesssim 5^\circ$ , respectively (144). **Figure 5** shows the light curve of a power-law structured jet model with  $E_j \approx 2 \times 10^{49}$  erg,  $\theta_j \approx 3^\circ$ , and  $n \approx 10^{-3} \text{ cm}^{-3}$  and with a viewing angle of  $\sim 21^\circ$ .

Another important observation that is likely related to the jet is GRB 170817A, detected 1.7 s after the merger (145), which is much weaker than the typical sGRB. This prompt  $\gamma$ -ray emission requires a relativistic motion of the emission region (146). The delay of the  $\gamma$ -ray detection from the merger indicates that the jet should be formed for  $\ll 1.7$  s after the merger. On the basis of numerical-relativity simulations, it has been suggested that a relativistic jet may be driven by magnetic fields after an MNS collapses to a BH (147) in a lifetime of  $\ll 1.7$  s. The collimation of the jet in GW170817 can be interpreted as follows. The jet interacts with the material ejected around the polar region before the jet breaks out from the ejecta surface. Consequently, the ejecta shocked by the jet form a cocoon, which helps collimation of the jet (148–150). The small opening angle of the jet in GW170817 indicates that an appreciable amount of ejecta is present around the polar region prior to jet formation (146).

**Figure 5** depicts models of the afterglow light curves arising from dynamical ejecta with an ISM of density  $n = 10^{-3} \text{ cm}^{-3}$ . If the microphysics parameters are somewhat optimistic, the radio

emission with a flux density of  $\sim 10 \mu\text{Jy}$  may be detectable in the near future. Also, we note that for future merger events, this radio emission may be a primary target for the radio-band observation, if the viewing angle of the merger events is sufficiently wide.

## DISCLOSURE STATEMENT

The authors are not aware of any affiliations, memberships, funding, or financial holdings that might be perceived as affecting the objectivity of this review.

## ACKNOWLEDGMENTS

We thank S. Fujibayashi, G. Hallinan, K. Ioka, M.M. Kasliwal, K. Kawaguchi, K. Kiuchi, K. Kyutoku, K.P. Mooley, E. Nakar, T. Piran, D. Radice, Y. Sekiguchi, M. Tanaka, and S. Wanajo for useful discussions. The writing of this review was supported by Grant-in-Aid for Scientific Research (16H02183) from the Japan Society for the Promotion of Science/Japanese Ministry of Education, Culture, Sports, Science and Technology. K.H. is supported by a Lyman Spitzer Jr. Fellowship in the Department of Astrophysical Science, Princeton University.

## LITERATURE CITED

1. Abadie J, et al. (LIGO Sci. Collab.). *Nucl. Instrum. Methods A* 624:223 (2010)
2. Accadia T, et al. (Virgo Collab.). *Class. Quantum Gravity* 28:025005 (2011). Erratum. *Class. Quantum Gravity* 28:079501 (2011)
3. Akutsu T, et al. *Prog. Theor. Exp. Phys.* 013:01 (2018)
4. Abbott BP, et al. *Phys. Rev. Lett.* 119:161101 (2017)
5. Lattimer JM, Schramm DN. *Astrophys. J. Lett.* 192:L145 (1974)
6. Eichler D, Livio M, Piran T, Schramm DN. *Nature* 340:126 (1989)
7. Thielemann F-K, Eichler M, Panov IV, Wehmeyer B. *Annu. Rev. Nucl. Part. Sci.* 67:253 (2017)
8. Davies MD, Benz W, Piran T, Thielemann F-K. *Astrophys. J.* 431:742 (1996)
9. Ruffert M, Janka H-T, Takahashi K, Schaefer G. *Astron. Astrophys.* 319:122 (1997)
10. Freiburghaus C, Rosswog S, Thielemann F-K. *Astrophys. J.* 525:L121 (1998)
11. Rosswog S, et al. *Astron. Astrophys.* 341:499 (1999)
12. Li L-X, Paczyński B. *Astrophys. J.* 507:L59 (1998)
13. Metzger BD, et al. *Mon. Not. R. Astron. Soc.* 406:2650 (2010)
14. Roberts LF, Kasen D, Lee WH, Ramirez-Ruiz E. *Astrophys. J.* 736:L21 (2011)
15. Goriely S, Bauswein A, Janka H-T. *Astrophys. J. Lett.* 738:L32 (2011)
16. Korobkin O, Rosswog S, Arcones A, Winteler C. *Mon. Not. R. Astron. Soc.* 426:1940 (2012)
17. Barnes J, Kasen D. *Astrophys. J.* 775:18 (2013)
18. Tanaka M, Hotokezaka K. *Astrophys. J.* 775:113 (2013)
19. LIGO Sci. Collab., et al. *Astrophys. J.* 848:L12 (2017)
20. Tanaka M, et al. *Pub. Astron. Soc. Jpn* 69:102 (2017)
21. Arcavi I, et al. *Nature* 551:64 (2017)
22. Coulter DA, et al. *Science* 358:1556 (2017)
23. Cowperthwaite PS, et al. *Astrophys. J. Lett.* 848:L17 (2017)
24. Drout MR, et al. *Science* 358:1570 (2017)
25. Evans PA, et al. *Science* 358:1565 (2017)
26. Kasliwal MM, et al. *Science* 358:1559 (2017)
27. Pian E, et al. *Nature* 551:67 (2017)
28. Smartt SJ, et al. *Nature* 551:75 (2017)
29. Tanvir NR, et al. *Astrophys. J. Lett.* 848:L27 (2017)

30. Nakar E, Piran T. *Nature* 478:82 (2011)
31. Shibata M. *Phys. Rev. D* 60:104052 (1999)
32. Shibata M, Uryū K. *Phys. Rev. D* 61:064001 (2000)
33. Duez MD, et al. *Class. Quantum Gravity* 27:114106 (2010)
34. Sekiguchi Y, Kiuchi K, Kyutoku K, Shibata M. *Phys. Rev. Lett.* 107:051102 (2011)
35. Deaton MB, et al. *Astrophys. J.* 776:47 (2013)
36. Foucart F, et al. *Phys. Rev. D* 90:024026 (2014)
37. Palenzuela C, et al. *Phys. Rev. D* 92:044045 (2015)
38. Sekiguchi Y, Kiuchi K, Kyutoku K, Shibata M. *Phys. Rev. D* 91:064059 (2015)
39. Foucart F, et al. *Phys. Rev. D* 94:123016 (2016)
40. Kiuchi K, et al. *Phys. Rev. D* 90:041502 (2014)
41. Kiuchi K, et al. *Phys. Rev. D* 92:124034 (2015)
42. Kiuchi K, et al. *Phys. Rev. D* 92:064034 (2015)
43. Hotokezaka K, et al. *Phys. Rev. D* 87:024001 (2013)
44. Foucart F, et al. *Phys. Rev. D* 87:084006 (2013)
45. Bauswein A, Goriely S, Janka H-T. *Astrophys. J.* 773:78 (2013)
46. Lovelace G, et al. *Class. Quantum Gravity* 30:135004 (2013)
47. Kyutoku K, Ioka K, Shibata M. *Phys. Rev. D* 88:041503(R) (2013)
48. Foucart F, et al. *Phys. Rev. D* 91:124021 (2015)
49. Foucart F, et al. *Phys. Rev. D* 93:044019 (2016)
50. Sekiguchi Y, et al. *Phys. Rev. D* 93:124046 (2016)
51. Lehner L, et al. *Class. Quantum Gravity* 33:184002 (2016)
52. Radice D, et al. *Mon. Not. R. Astron. Soc.* 460:3255 (2016)
53. Foucart F, et al. *Class. Quantum Gravity* 34:044002 (2017)
54. Kyutoku K, et al. *Phys. Rev. D* 97:023009 (2018)
55. Dietrich T, et al. *Phys. Rev. D* 95:024029 (2017)
56. Dietrich T, Bernuzzi S, Ujevic M, Tichy W. *Phys. Rev. D* 95:044045 (2017)
57. Bovard L, et al. *Phys. Rev. D* 96:124005 (2017)
58. Radice D, et al. *Astrophys. J.* 869:130 (2018)
59. Wanajo S, et al. *Astrophys. J. Lett.* 789:L39 (2014)
60. Fernández R, et al. *Class. Quantum Gravity* 34:154001 (2017)
61. Fernández R, Metzger BD. *Mon. Not. R. Astron. Soc.* 435:502 (2013)
62. Metzger BD, Fernández R. *Mon. Not. R. Astron. Soc.* 441:3444 (2014)
63. Perego A, et al. *Mon. Not. R. Astron. Soc.* 443:3134 (2014)
64. Fernández R, Kasen D, Metzger BD, Quataert E. *Mon. Not. R. Astron. Soc.* 446:750 (2015)
65. Just O, et al. *Mon. Not. R. Astron. Soc.* 448:541 (2015)
66. Siegel DM, Metzger BD. *Phys. Rev. Lett.* 119:231102 (2017)
67. Fujibayashi S, et al. *Astrophys. J.* 860:64 (2018)
68. Fernández R, et al. *Mon. Not. R. Astron. Soc.* 482:3373 (2019)
69. Baumgrate TW, Shapiro SL, Shibata M. *Astrophys. J. Lett.* 528:L28 (2000)
70. Shibata M. *Numerical Relativity*. Singapore: World Sci. (2016)
71. Shibata M, Taniguchi K, Uryū K. *Phys. Rev. D* 71:084021 (2005)
72. Shibata M, Taniguchi K. *Phys. Rev. D* 73:064027 (2006)
73. Kiuchi K, Sekiguchi Y, Shibata M, Taniguchi K. *Phys. Rev. D* 80:064037 (2009)
74. Hotokezaka K, et al. *Phys. Rev. D* 83:124008 (2011)
75. Hotokezaka K, et al. *Phys. Rev. D* 88:044026 (2013)
76. Takami K, Rezzolla L, Baiotti L. *Phys. Rev. D* 91:064001 (2015)
77. Dietrich T, Bernuzzi S, Ujevic M, Brüggmann B. *Phys. Rev. D* 91:124041 (2015)
78. Bernuzzi S, et al. *Phys. Rev. D* 94:024023 (2016)
79. Ciolfi R, et al. *Phys. Rev. F* 95:063016 (2017)
80. Demorest PB, et al. *Nature* 467:1081 (2010)
81. Antoniadis J, et al. *Science* 340:448 (2013)

82. Tauris TM, et al. *Astrophys. J.* 846:170 (2017)
83. Pol N, McLaughlin M, Lorimer DR. arXiv:1811.04086 [astro-ph.HE] (2018)
84. Balbus SA, Hawley JF. *Rev. Mod. Phys.* 70:1 (1998)
85. Meszaros P, Rees MJ. *Astrophys. J.* 397:570 (1992)
86. Ruffert M, Janka H-T. *Astron. Astrophys.* 344:573 (1996)
87. Di Matteo T, Perna R, Narayan R. *Astrophys. J.* 579:706 (2002)
88. Lee WH, Ramirez-Ruiz E, Page D. *Astrophys. J.* 632:421 (2005)
89. Setiawan S, Ruffert M, Janka H-T. *Mon. Not. R. Astron. Soc.* 352:753 (2004)
90. Shibata M, Sekiguchi Y, Takahashi R. *Prog. Theor. Phys.* 118:257 (2007)
91. Chen W-X, Beloborodov AM. *Astrophys. J.* 657:383 (2007)
92. Blandford RD, Znajek RL. *Mon. Not. R. Astron. Soc.* 179:433 (1977)
93. McKinney JC. *Mon. Not. R. Astron. Soc.* 368:1561 (2006)
94. Paschalidis V, Ruiz M, Shapiro SL. *Astrophys. J.* 806:L14 (2015)
95. Ruiz M, Lang RN, Paschalidis V, Shapiro SL. *Astrophys. J.* 824:L6 (2016)
96. Duez MD, Liu Y-T, Shapiro SL, Stephens BC. *Phys. Rev. D* 69:104030 (2004)
97. Shibata M, Kiuchi K, Sekiguchi Y. *Phys. Rev. D* 95:083005 (2017)
98. Price DJ, Rosswog S. *Science* 312:719 (2006)
99. Kiuchi K, et al. *Phys. Rev. D* 97:124039 (2018)
100. Chandrasekhar S. *Hydrodynamic and Hydromagnetic Stability*. Oxford, UK: Oxford Univ. Press (1961)
101. Shakura NI, Sunyaev RA. *Astron. Astrophys.* 24:337 (1973)
102. Hawley JF, Richers SA, Guan X, Krolik JH. *Astrophys. J.* 772:102 (2013)
103. Suzuki TK, Inutsuka S. *Astrophys. J.* 784:121 (2014)
104. Shi JM, Stone JM, Huang CX. *Mon. Not. R. Astron. Soc.* 456:2273 (2016)
105. Friedman JL, Ipser JR, Parker L. *Astrophys. J.* 304:115 (1986)
106. Cook GB, Shapiro SL, Teukolsky SA. *Astrophys. J.* 423:823 (1994)
107. Shibata M, Uryū K. *Phys. Rev. D* 74:121503(R) (2006)
108. Kyutoku K, Shibata M, Taniguchi K. *Phys. Rev. D* 82:044049 (2010)
109. Kyutoku K, Okawa H, Shibata M, Taniguchi K. *Phys. Rev. D* 84:064018 (2011)
110. Foucart F, Duez MD, Kidder LE, Teukolsky SA. *Phys. Rev. D* 83:024005 (2012)
111. Foucart F, et al. *Phys. Rev. D* 85:044015 (2012)
112. Kawaguchi K, et al. *Phys. Rev. D* 92:024014 (2015)
113. Kyutoku K, et al. *Phys. Rev. D* 92:044028 (2015)
114. Hotokezaka K, et al. *Astrophys. J.* 867:95 (2018)
115. Lippuner J, Roberts LF. *Astrophys. J.* 815:82 (2015)
116. Kasen D, Fernández R, Metzger BD. *Mon. Not. R. Astron. Soc.* 450:1777 (2015)
117. Lippuner J, et al. *Mon. Not. R. Astron. Soc.* 472:904 (2017)
118. Qian Y-Z, Woosley SE. *Astrophys. J.* 471:331 (1996)
119. Hotokezaka K, Sari R, Piran T. *Mon. Not. R. Astron. Soc.* 468:91 (2017)
120. Wu M-R, Barnes J, Martinez-Pinedo G, Metzger BD. arXiv:1808.10459 [astro-ph] (2018)
121. Hotokezaka K, et al. *Mon. Not. R. Astron. Soc.* 459:35 (2016)
122. Zhu Y, et al. *Astrophys. J. Lett.* 863:L23 (2018)
123. Barnes J, Kasen D, Wu M-R, Martinez-Pinedo G. *Astrophys. J.* 829:110 (2016)
124. Kasen D, Barnes J. arXiv:1807.03319 [astro-ph] (2018)
125. Waxman E, Ofek E, Kushnir D, Gal-Yam A. *Mon. Not. R. Astron. Soc.* 481:3423 (2018)
126. Kasen D, Badnell NR, Barnes J. *Astrophys. J.* 774:25 (2013)
127. Tanaka M, et al. *Astrophys. J.* 852:109 (2018)
128. Wollaeger RT, et al. *Mon. Not. R. Astron. Soc.* 478:3298 (2018)
129. Villar AA, et al. *Astrophys. J. Lett.* 851:L21 (2017)
130. Nakar E, et al. *Astrophys. J.* 867:18 (2018)
131. Hotokezaka K, et al. *Astrophys. J.* 831:190 (2016)
132. Arcavi I. *Astrophys. J.* 855:L23 (2018)
133. Kasliwal MM, et al. *Mon. Not. R. Astron. Soc.* In press. <https://doi.org/10.1093/mnrasl/slz007> (2019)

134. Kasen D, et al. *Nature* 551:7678 (2017)
135. Perego A, Radice D, Bernuzzi S. *Astrophys. J. Lett.* 850:L37 (2017)
136. Shibata M, et al. *Phys. Rev. D* 96:123012 (2017)
137. Kawaguchi K, Shibata M, Tanaka M. *Astrophys. J. Lett.* 865:L21 (2018)
138. Troja E, et al. *Nature* 551:71 (2017)
139. Hallinan G, et al. *Science* 358:6370 (2017)
140. Mooley KP, et al. *Nature* 554:7691 (2018)
141. Troja E, et al. *Mon. Not. R. Astron. Soc.* 487:L18 (2018)
142. Mooley KP, et al. *Astrophys. J. Lett.* 868:L21 (2018)
143. Margutti R, et al. *Astrophys. J. Lett.* 856:L18 (2018)
144. Mooley KP, et al. *Nature* 561:7723 (2018)
145. Abbott BP, et al. *Astrophys. J. Lett.* 848:L13 (2017)
146. Gottlieb O, Nakar E, Piran T, Hotokezaka K. *Mon. Not. R. Astron. Soc.* 479:588 (2018)
147. Ruiz M, Shapiro SL. *Phys. Rev. D* 96:084063 (2017)
148. Nagakura H, Hotokezaka K, Sekiguchi Y, Shibata M. *Astrophys. J. Lett.* 784:L28 (2014)
149. Murguia-Berthier A, et al. *Astrophys. J. Lett.* 788:L8 (2014)
150. Duffell PC, Quataert E, MacFadyen AI. *Astrophys. J.* 813:64 (2015)